remote sensing

MDPI

Article

Dynamics of the Net Precipitation in China from 2001 to 2020

Jing Pan [1,2], Yongyue Ji [1,2], Lingyun Yan [1,2], Yixia Luo [1,2] and Jilong Chen [1,*]

[1] Chongqing Institute of Green and Intelligent Technology, Chinese Academy of Sciences, Chongqing 400714, China; panjing@cigit.ac.cn (J.P.); jiyongyue@cigit.ac.cn (Y.J.); yanlingyun@cigit.ac.cn (L.Y.); luoyixia@cigit.ac.cn (Y.L.)
[2] University of Chinese Academy of Sciences, Beijing 100049, China
* Correspondence: chenjilong@cigit.ac.cn

Abstract: Net precipitation (NP) is the primary source of soil water essential for the functioning of vegetated ecosystems. By quantifying NP as the difference between gross precipitation and canopy interception evaporation, this study examined the dynamics of NP in China from 2001 to 2020 and the contribution of environmental factors to NP variations was investigated. The findings revealed a multiyear mean NP of 674.62 mm, showcasing a 2.93 mm/yr increase. The spatiotemporal variations in NP were mainly attributed to a remarkable increase in precipitation rather than canopy interception. Notably, climate (temperature, wind speed, surface solar radiation downward and vapor pressure deficit) and vegetation factors (leaf area index and net primary productivity) played a dominant role in NP in 61.53% and 15.39% of China, respectively. The dominant factors contributing to NP changes were vapor pressure deficit (mean contribution rate: −43.68%), temperature (mean contribution rate: 11.69%), and leaf area index (mean contribution rate: 2.13%). The vapor pressure deficit negatively exerts a negative influence on the southern and eastern regions. Temperature and leaf area index have the greatest effect on the northeastern and southwestern regions, respectively. The results provide valuable insights into the pivotal role of climatic and vegetation factors in ecohydrological cycles.

Keywords: net precipitation; rainfall redistribution; climate change; vegetation factors; China

Citation: Pan, J.; Ji, Y.; Yan, L.; Luo, Y.; Chen, J. Dynamics of the Net Precipitation in China from 2001 to 2020. *Remote Sens.* **2024**, *16*, 2094. https://doi.org/10.3390/rs16122094

Academic Editors: Simone Lolli, Qiang Zhang, Yu Zhang, Ping Yue, Zesu Yang and Yongli He

Received: 4 March 2024
Revised: 2 June 2024
Accepted: 6 June 2024
Published: 10 June 2024

1. Introduction

When precipitation falls on a vegetated surface, a portion is intercepted by the canopy and evaporates directly back into the atmosphere (interception) [1–3]. The remaining water reaches the ground via two distinct pathways: throughfall (Tf), which occurs when water passes through the canopy gaps and drips off, and stemflow (Sf), which refers to the flow of water drained to an individual plant's stem base [4,5]. The effective amount of water that ultimately reaches the ground is termed net precipitation (NP), representing the sum of Tf and Sf [5,6]. The redistribution of rainfall at the ground surface gives rise to variability in the amount and spatiotemporal pattern of NP observations at the surface when compared to precipitation that falls on the top of the canopy. Generally, NP is less than gross precipitation above the canopy, except during cloud or fog events [7], due to water storage and evaporation [5]. The redistribution process enhances the spatiotemporal variation in NP by altering the horizontal and vertical distribution of water [4,8,9]. It affects soil moisture patterns [10], nutrient budgets [11], and localized preferential flow [12] within vegetated ecosystems. Therefore, comprehending the characteristics of NP is crucial for advancing our understanding of hydrologic and biogeochemical processes [6].

The measurement of NP has typically been conducted by directly measuring Tf and Sf [2,5]. These measurements are typically taken at specific points during both liquid and frozen precipitation events [13–15], using capture devices designed for this purpose [16,17]. The overwhelming majority of NP studies have been conducted at the field plot scale and focused on individual plant species or mixed species at specific sites [18–20]. These

studies have greatly improved our understanding of the fine or local scale of rainfall partitioning processes and contribute a wealth of data that can be used for comprehensive synthesis at larger scales. Particularly in recent years, some studies have synthesized and analyzed observations of Tf and/or Sf from independent publications in order to quantify the patterns of NP by vegetation at regional or global scales [4,5,9,18,21]. Previous studies have indicated that the median levels of relative Tf and Sf globally are approximately 75% and 3% of total rainfall, respectively [5,9]. Although these syntheses provided information about the general pattern at a large scale, the number of observations at certain sites is insufficient, resulting in a gap in data for NP in low vegetation and mixed precipitation events [22–24].

A multitude of studies have demonstrated that NP is significantly influenced by meteorological conditions and vegetation characteristics. In particular, precipitation exerts a direct influence on NP, as storm magnitude determines the canopy storage capacity, while storm intensity can influence the time to saturation [2,19]. The stand-scale NP shows marked variation in relation to the characteristics of the dominant and understory vegetation [25]. NP was found to decrease in leafless conditions [26] and to be strongly correlated with leaf area index (LAI) for herbaceous plants [27,28]. Consequently, alterations in the states of leaves throughout the seasons and associated fluctuations in precipitation conditions can also exert a considerable influence on NP [29]. Furthermore, other factors, such as temperature, sunshine duration, humidity, and wind speed, also exert some influence on the variability of NP to some extent. The majority of current studies focus on the fine-scale drivers that shape highly localized patterns [5]. Nevertheless, the aforementioned studies did not perform a quantitative analysis of the impact and relative importance of potential drivers, which limits the accuracy of large-scale predictions under changing climate conditions.

China, endowed with extensive and diverse topography and climate types, harbors a rich and intricately complex variety of vegetation characterized by uneven precipitation distribution [30]. The phenomena observed in China, including greening [31,32], increasing precipitation variability [33,34], and shifts in land use [24,35,36], significantly influence the stages of precipitation redistribution. Although many field experiments are conducted at the site level or in typical ecosystems [18,37–39], there is a lack of large-scale maps of NP in China and qualifications of the contribution of climate and vegetation factor influence on NP over past two decades. Our study leveraged large-scale evaporation of canopy interception (EI) products and models, enabling us to indirectly map NP as the difference between gross precipitation and EI. This approach is made possible by the Penman–Monteith–Leuning (PML) model [40–42], which has been further refined by Zhang et al. [43]. By employing this model, we aim to explore NP patterns in China and investigate the macroscale role of precipitation–vegetation interactions on NP over a long-term period. The main objectives of this study are to (1) characterize the spatiotemporal dynamics across China from 2001 to 2020; (2) quantify the contributions of climate and vegetation factors to determine the most influential factors on spatiotemporal changes in NP. Our study offers a new perspective and a tool that can be used alongside field measurements to enhance our knowledge of water balance dynamics, contributing valuable insights into the effects of China's greening and climate change on water and energy exchange.

2. Materials and Methods

2.1. Data Collection

EI (mm) data used to calculate NP were sub datasets from the global PML-V2 Evapotranspiration (ET) datasets, which had an 8-day temporal resolution and a spatial resolution of 500 m. Zhang et al. [44] included EI to estimate the three components of ET across the globe and Zhang et al. [43] extensively calibrated the PML-V2 model using data from 95 flux towers for 10 plant functional types worldwide. The PML-V2 EI product for China from 2001 to 2020 was obtained from the Google Earth Engine (GEE) platform (https://

developers.google.com/earth-engine/datasets/catalog/CAS_IGSNRR_PML_V2_v017, accessed on 17 June 2023).

The meteorological data, including gross precipitation (PRE, mm), air temperature (TEM, °C), wind speed (WIN, m/s) and relative humidity (RH, %), were obtained from the China National Ground Meteorological Station Basic Meteorological Elements Daily Values Dataset (V3.0) (http://data.cma.cn/, accessed on 21 July 2023). Annual cumulative values were calculated for PRE, and annual mean values were calculated for TEM and WIN. These annual values were then interpolated into gridded data using the ANUSPLIN 4.37 software for improved spatial analysis capabilities. Yearly surface solar radiation downward (SSRD, W/m^2) data were derived from the European Centre for Medium-Range Weather Forecasts (ECMWF) ERA5-Land reanalysis dataset (https://www.ecmwf.int/en/era5-land, accessed on 23 July 2023). Vapor Pressure Deficit (VPD, kPa) was calculated using a specific equation.

$$\mathrm{VPD} = 0.61078 \times e^{\frac{17.27 \times \mathrm{TEM}}{\mathrm{TEM}+237.3}} \times (1 - \mathrm{RH}) \quad (1)$$

Vegetation factors including LAI and net primary productivity (NPP) data were obtained from MODIS products (MOD15A2H and MOD17A3) with 500 m and 8-day resolution, processed into annual datasets using the GEE platform.

The physical geographic division data of China, including the vegetation regionalization map, moisture regions, and land-use types, were obtained from the Resource and Environment Science and Data Center (https://www.resdc.cn, accessed on 21 June 2023). Overall, China was divided into the following eight vegetation regions: I (cold temperate coniferous forest), II (temperate mixed coniferous and broad-leaved forest), III (warm temperate deciduous broad-leaved forest), IV (sub-tropical evergreen broad-leaved forest), V (tropical monsoon forest), VI (temperate grassland), VII (temperate desert), and VIII (alpine vegetation). The physical geographic division is presented in Figure 1a. Furthermore, the land use in China was classified into six categories, as illustrated in Figure 1b.

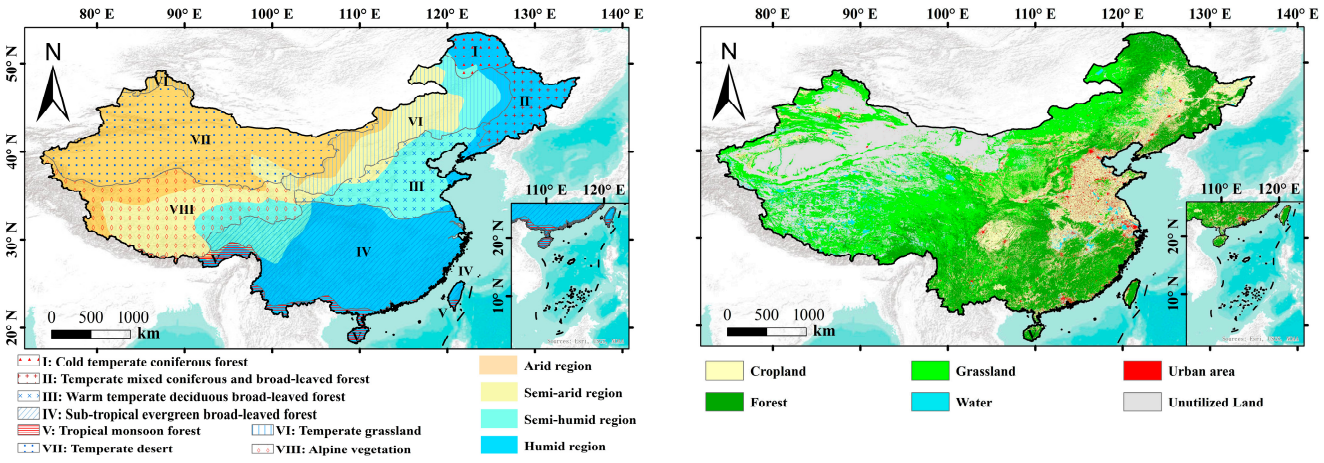

(**a**) (**b**)

Figure 1. Location of (**a**) eight vegetation type regions and (**b**) six land-use types in China.

The time series for all datasets spanned from 2001 to 2020, covering China. For subsequent analysis, all data were processed using a spatial resolution of approximately 1 km and projected to the same coordinate system (GCS_WGS_1984). This spatial resolution was determined based on the coarsest spatial resolution among all datasets.

2.2. Methodology

2.2.1. Calculations of NP

In accordance with the process of rainfall partitioning by vegetation, NP was calculated as the difference between annual PRE and annual EI [1,38,45]. The estimation of NP at large scales was calculated as follows:

$$NP = PRE - EI = Tf + Sf \quad (2)$$

2.2.2. Trend Analysis

The temporal trends of NP were determined using linear regression at the national, regional, and pixel levels. The trends were calculated as follows:

$$TR_{NP} = \frac{n\sum_{i=1}^{n} ix_i - \sum_{i=1}^{n} i\sum_{i=1}^{n} x_i}{n\sum_{i=1}^{n} i^2 - \left(\sum_{i=1}^{n} i\right)^2} \quad (3)$$

where n is the length of research years, x_i is the ith year of NP, and TR_{NP} is the long-term NP trend in China from 2001 to 2020. $TR_{NP} > 0$ indicates an increasing trend, while $TR_{NP} < 0$ indicates a decreasing trend. Moreover, the F-test was conducted to test the significance of slope in this study, where $0.01 \leq p < 0.05$ stands for statistically significant, $p < 0.01$ stands for highly significant and $p \geq 0.05$ stands for not significant.

2.2.3. Contribution Analysis

The contributions of PRE and EI to the NP trends were quantified using a differential equation [46,47]. PRE represented the influence of the precipitation regime, whereas EI signified the impact of water interception by plants on NP. As NP varied with time, the long-time trend of NP was calculated as follows:

$$\frac{dNP}{dt} = \frac{\partial NP}{\partial PRE_i}\frac{dPRE_i}{dt} - \frac{\partial NP}{\partial EI_i}\frac{dEI_i}{dt} + \varepsilon \quad (4)$$

Equation (4) could also be rewritten as follows:

$$TR_{NP} = C(PRE) + C(EI) + \varepsilon \quad (5)$$

where C(PRE) and C(EI) are the contributions of PRE and EI to the long-time trend of NP, respectively. ε is the system error.

The relative contribution rate of PRE (CR(PRE)) and EI (CR(EI)) were calculated as follows:

$$CR(PRE) = \frac{C(PRE)}{C(PRE)+C(EI)} \times 100\% \quad (6)$$

$$CR(EI) = \frac{C(EI)}{C(PRE)+C(EI)} \times 100\% \quad (7)$$

Furthermore, to separate the individual contributions of climatic factors (TEM, WIN, SSRD and VPD) and vegetation factors (LAI and NPP), the Elastic Net Regression model was employed at the pixel grid. The model utilized the annual average values of these variables from 2001 to 2020 for each raster cell, thereby ensuring the precision and reliability of the outcomes. The model exhibited robustness against multicollinearity and facilitated variable selection [48,49]. The model can be expressed as follows:

$$\min_{\{\beta_0,\beta_1,\beta_2,\ldots,\beta_p\}} \left[\sum_{i=1}^{n}\left(Y_i - \beta_0 - \sum_{j=1}^{p}\beta_j X_{ij}\right)^2 - \lambda\left(\alpha\sum_{j=1}^{p}\left|\beta_j\right| + \frac{1-\alpha}{2}\sum_{j=1}^{p}\beta_j^2\right)\right] \quad (8)$$

where i = 1, 2, . . . n (a total of n grids); j = 1, 2 . . . p (p = 6, means six independent variables); X was the standardized value of independent variables; Y was equal to the standardized value of NP; β was the regression coefficient and β0 was the intercept coefficient; α was

the mixing parameter, which determined the balance between L1(α = 0) and L2(α = 1) regularization. In this study, α = 0.5 was chosen to ensure effective contributor selection and strong robustness. λ was the hyperparameter that controlled the strength of regularization and the optimal value of λ depended on the performance of cross-validation.

The coefficients obtained (β_1, β_2, . . ., β_p) were used to build the regression model to assess the contributions of independent variables to the dependent variable. The individual driver's relative contribution rate was expressed accordingly, with the positive and negative signs determined by the original coefficients. The R package glmnet was used to complete the build the regression model.

$$CR(X_i) = \frac{\beta_j}{\sum_{j=1}^{p} |\beta_j|} \quad (9)$$

Path analysis was employed in this study since it could effectively decompose the correlation between the independent and dependent variables in cases where there were complex interactions between the independent variables or the independent variable indirectly affected the independent variable through other independent variables [35]. The magnitude of the path coefficient indicated the impact of the independent variable on the dependent variable, with its sign denoting positivity or negativity. The R package lavaan conducted the path analysis in this study.

3. Results

3.1. Dynamics of NP in China from 2001 to 2020

3.1.1. Spatiotemporal Variation in Mean NP

The multiyear mean NP (Figure 2a) from 2001 to 2020 exhibited a significant gradient, decreasing from the southeast to the northwest in China. The national mean value of multiyear annual NP was 674.62 mm, with a range of 3.23 mm to 4694.25 mm (Figure 2a). Regions with high NP values (>1000 mm) were concentrated in the southeastern parts of China, particularly along the coastal regions. In contrast, arid and lowland terrains in northeastern China had low NP values (<200 mm). At the regional level, region V had the highest annual NP with a mean value of 1376.47 mm, followed by region IV with a mean value of 1115.30 mm (Figure 2c). On the other hand, region VII had the lowest annual NP with only 227.95 mm (Figure 2c). The remaining regions had annual mean NP values ranging from 344.82 mm to 603.56 mm (Figure 2c).

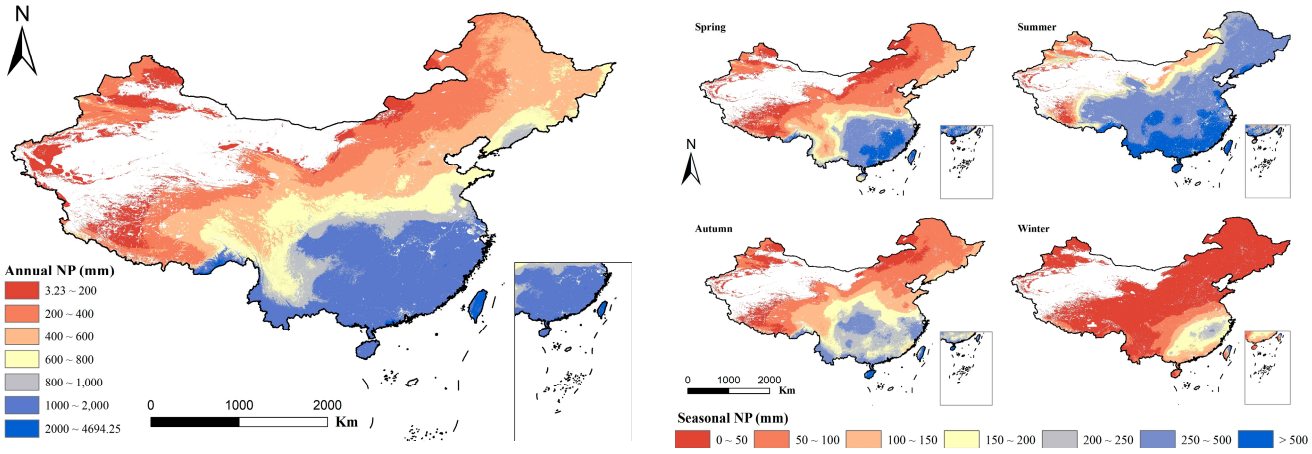

(**a**) (**b**)

Figure 2. *Cont.*

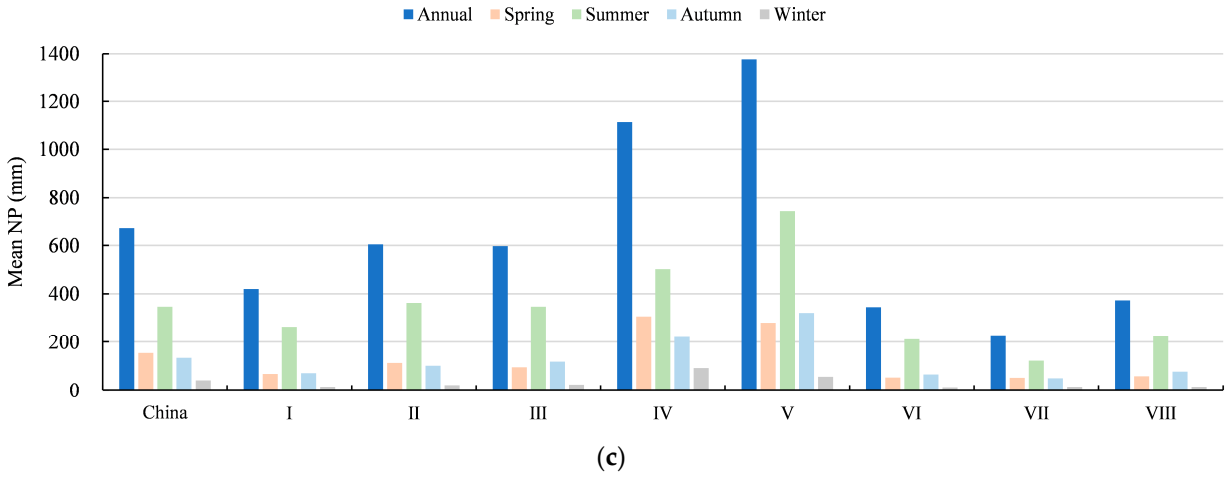

(**c**)

Figure 2. (**a**) Spatial distribution of the multiyear mean annual NP and (**b**) seasonal NP; (**c**) the multiyear mean value of NP in China and 8 vegetation-type regions. I: cold temperate coniferous forest, II: temperate mixed coniferous and broad-leaved forest, III: warm temperate deciduous broad-leaved forest, IV: sub-tropical evergreen broad-leaved forest, V: tropical monsoon forest, VI: temperate grassland, VII: temperate desert, and VIII: alpine vegetation (the same as below).

On a seasonal scale, NP exceeds 200 mm in summer in most semi-humid and humid regions, with some southwestern humid regions also reaching this threshold in spring and autumn (Figure 2b). In contrast, arid and semi-arid regions have NP values consistently below 100 mm per year (Figure 2b). The multi-year seasonal mean NP in China peaks in summer (346.56 mm), followed by spring (154.18 mm), autumn (134.24 mm) and is lowest in winter (42.67 mm) (Figure 2c).

Figure 3a shows a contrasting spatial pattern in the percentage of NP/PRE. The NP/PRE ratio was low in humid and semi-humid regions and reached its lowest point in the northeast region and differed across seasons. The percentage of NP/PRE across China fluctuated between 30.85% and 100%, with an average value of 94.89% (Figure 3c). Region I had the lowest percentage of NP/PRE at 85.58%, while the remaining seven regions had higher values, ranging from 92.54% to 97.93%. At the seasonal scale (Figure 3b), the region with the greatest canopy interpretation differed from the other regions. In spring, the Yunan and Hainan provinces exhibited the lowest NP/PRE. In summer, region I and the majority of region IV exhibited low NP/PRE values. In autumn, the southern regions of region IV exhibited low NP/PRE values. In winter, the lowest NP/PRE values were observed in regions IV and V, particularly in Yunnan and the southern coastal cities.

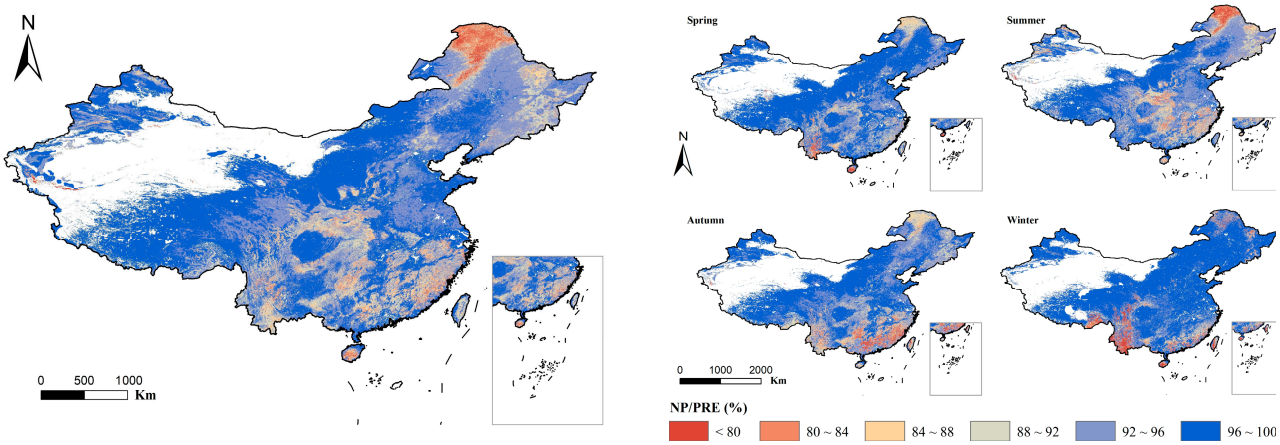

(**a**) (**b**)

Figure 3. *Cont.*

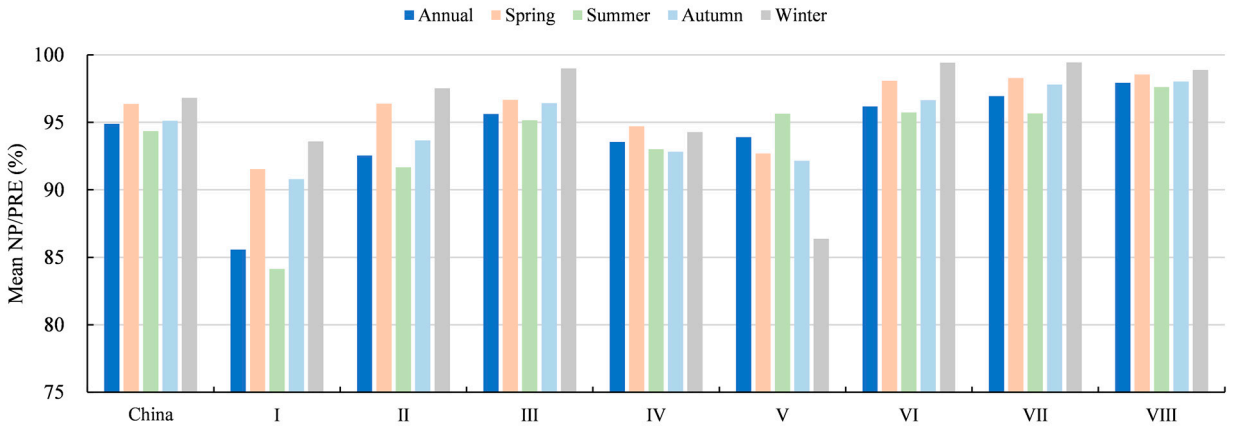

(**c**)

Figure 3. (**a**) Spatial distribution of the multiyear mean annual NP/PRE and (**b**) seasonal NP/PREE; (**c**) the multiyear mean NP/PRE of China and each region.

3.1.2. Spatiotemporal Trend of NP

The annual mean NP in China exhibited a significant upward trend of 2.93 mm/yr ($p < 0.05$) with regional variations (Figure 4). Notably, only region V was characterized by a decreasing trend (−3.91 mm/yr), while seven other regions displayed an increasing trend in annual mean NP. These upward trends ranged from 0.48 (region VIII) to 7.35 mm/yr (region II). In seasonal terms (Figure 4), summer and autumn exhibited a highly significant ($p < 0.01$) and significant ($p < 0.05$) increasing trend in mean NP values, respectively, at 2.24 mm/yr and 1.43 mm/yr. Conversely, spring and winter displayed a non-significant downward trend in seasonal mean NP. The change in annual NP indicated that 75.96% of China had experienced an increase, while 24.04% had witnessed a decrease (Figure 5). Within this context, 3.63% of the whole area of China demonstrated a highly significant increase ($p < 0.01$), particularly in the Sichuan basin and the mountain range in the northeastern section. Conversely, the decreasing trend was mainly concentrated in China's southern border, spanning from southeastern Tibet and southern Yunnan to southwestern Guangxi, predominantly south of 22°30′N latitude.

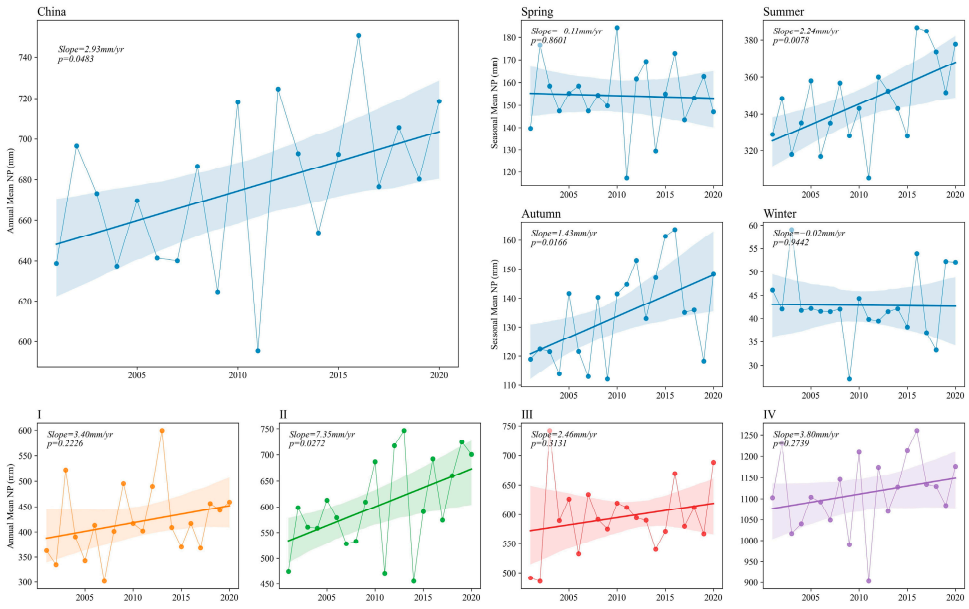

Figure 4. *Cont.*

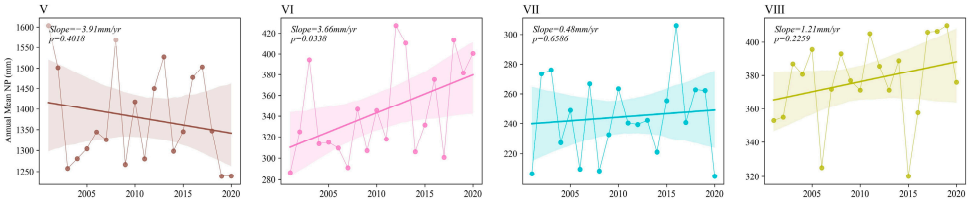

Figure 4. Annual and seasonal mean NP trends in China across 8 vegetation types and 4 seasons.

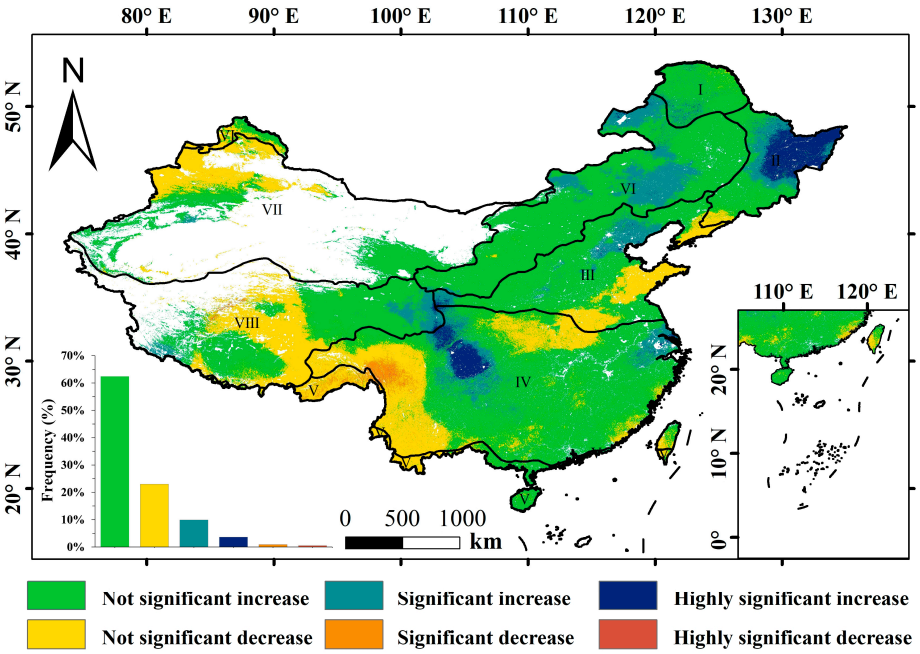

Figure 5. Spatial patterns of NP trend in China.

3.2. Potential Drivers of Spatiotemporal Variation in NP

3.2.1. Contribution of PRE and EI in Controlling NP Trend

From 2001 to 2020, both PRE and EI exhibited rising trends at rates of 3.39 mm/yr and 1.63 mm/yr, respectively (Figure 6). Analysis of their contributions to the overall NP trends revealed that PRE provides significant and positive contributions, while EI played a secondary role, contributing negatively at 32.45% (Figure 6). On a national scale (Figure 7), NP trends in the majority of regions (72.95%) were dominated by PRE. Only a small percentage of regions were primarily influenced by EI, concentrated in the Hanzhong Basin in region IV, the North China Plain in region III, and the Dzungarian Basin in region VII. The NP trend in these regions was dominated by EI, resulting in patterns resembling meandering curves and circles along mountain ranges due to the influence of elevation and climate. At the regional level (Figure 6), PRE accounted for more than 60% of the contributions. Specifically, values in regions VIII and V were over 70%, with the highest value reaching 82.52% in region I. Similar contributions of PRE and EI to the NP trend were only observed in region VII.

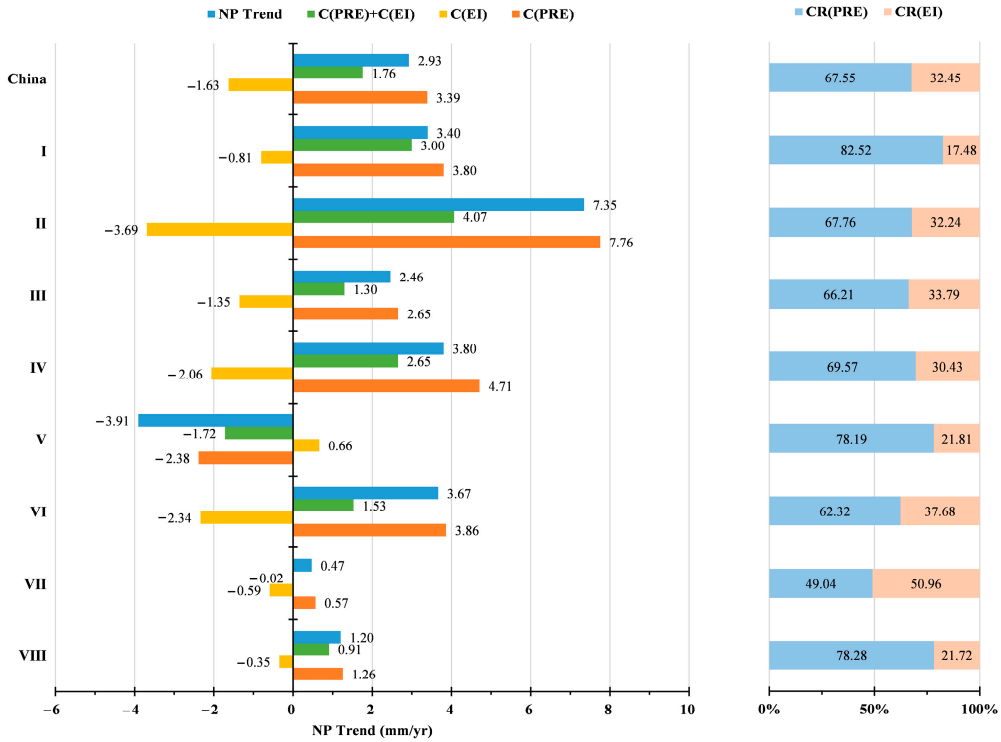

Figure 6. Contributions and contribution rates of PRE and EI to NP trends in China and each region.

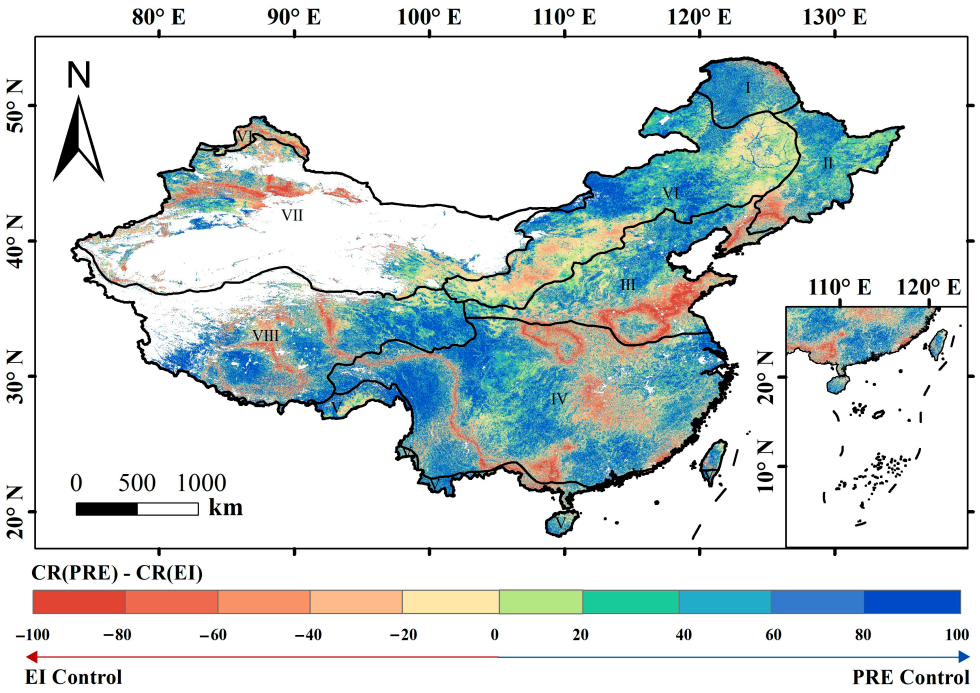

Figure 7. Spatial patterns of PRE and EI contribution rates to NP trends in China.

3.2.2. Climate and Vegetation Potential Drivers in NP Variation

The Elastic Net Regression analysis revealed substantial spatial variability in the contributions of various factors to NP at the national scale (Figure 8). TEM (Figure 8c) was identified as the principal positive driver, contributing to NP changes in China with a mean contribution rate of 11.69% (Figure 9), and exerted a predominant role in 15.04% of the country's area (Figure 10). It is noteworthy that in regions III and VI, its contribution rate exceeded 20% (Figure 9).

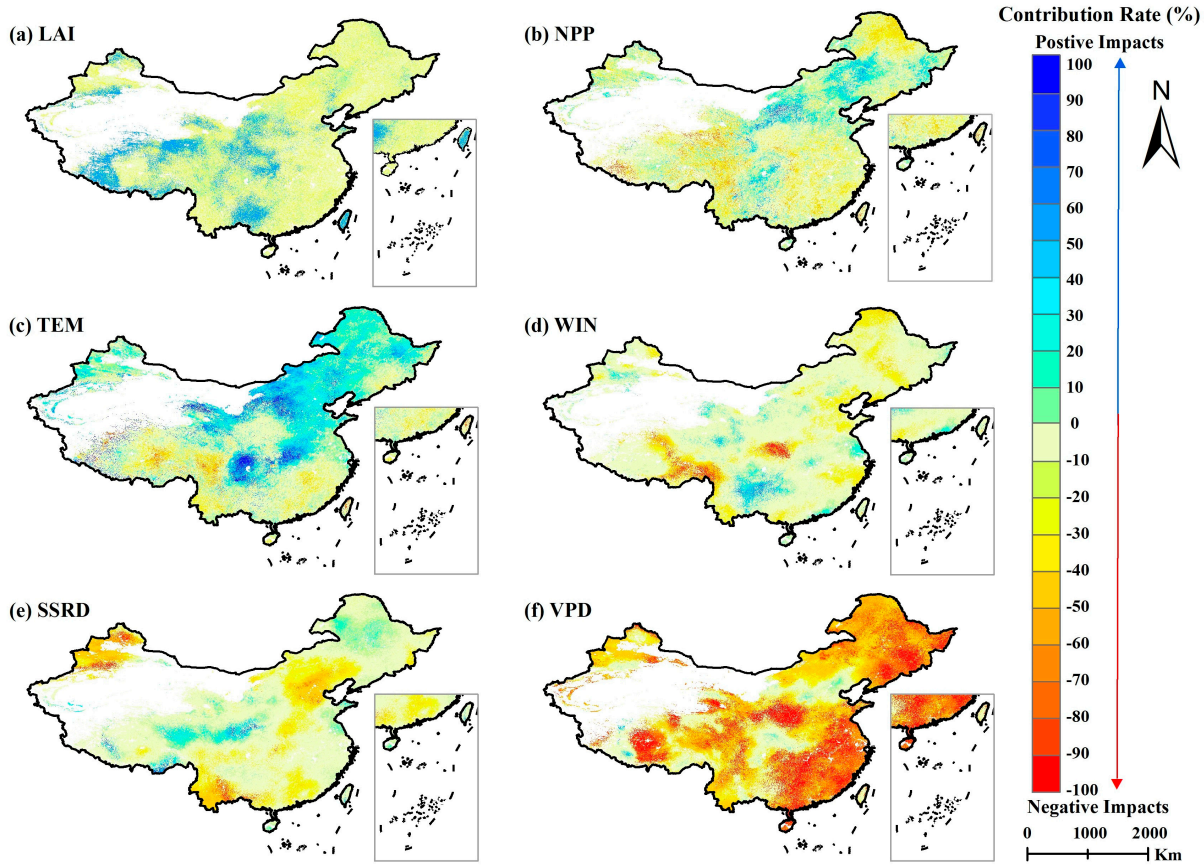

Figure 8. Spatial patterns of relative contribution rates of (**a**) LAI, (**b**) NPP, (**c**) TEM, (**d**) WIN, (**e**) SSRD and (**f**) VPD to NP changes in China.

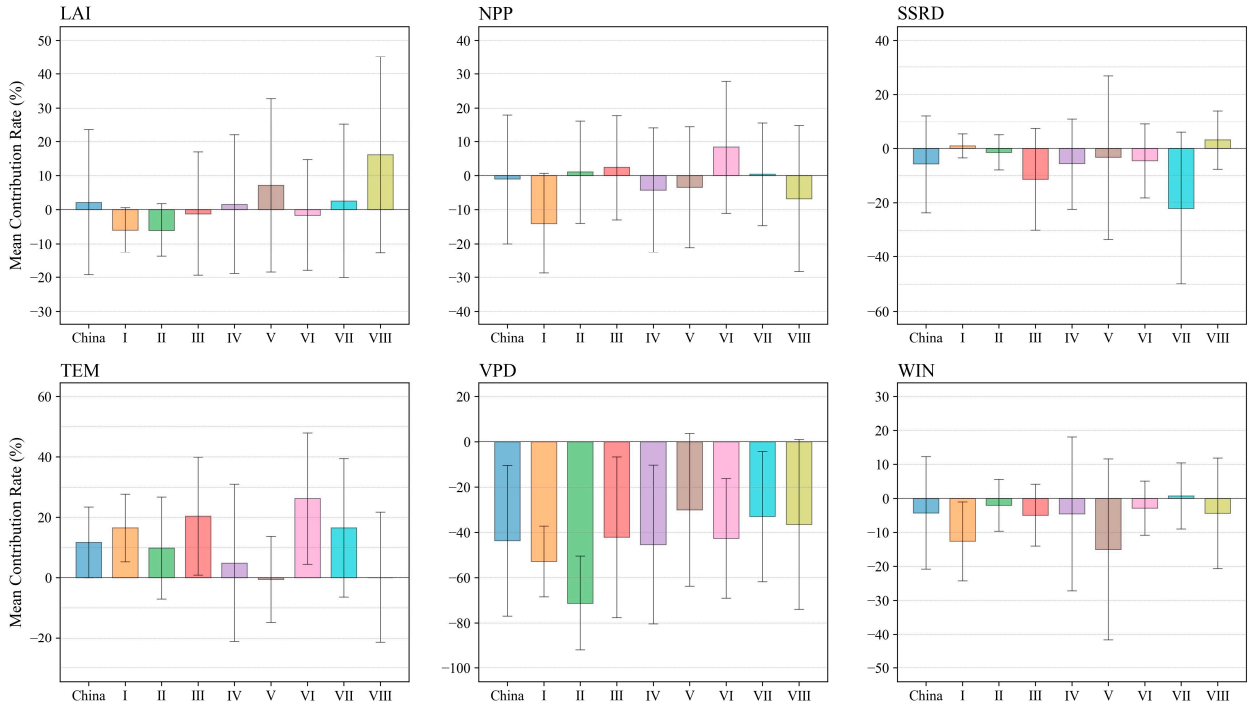

Figure 9. Regional-averaged contribution rates of each factor in China and each region.

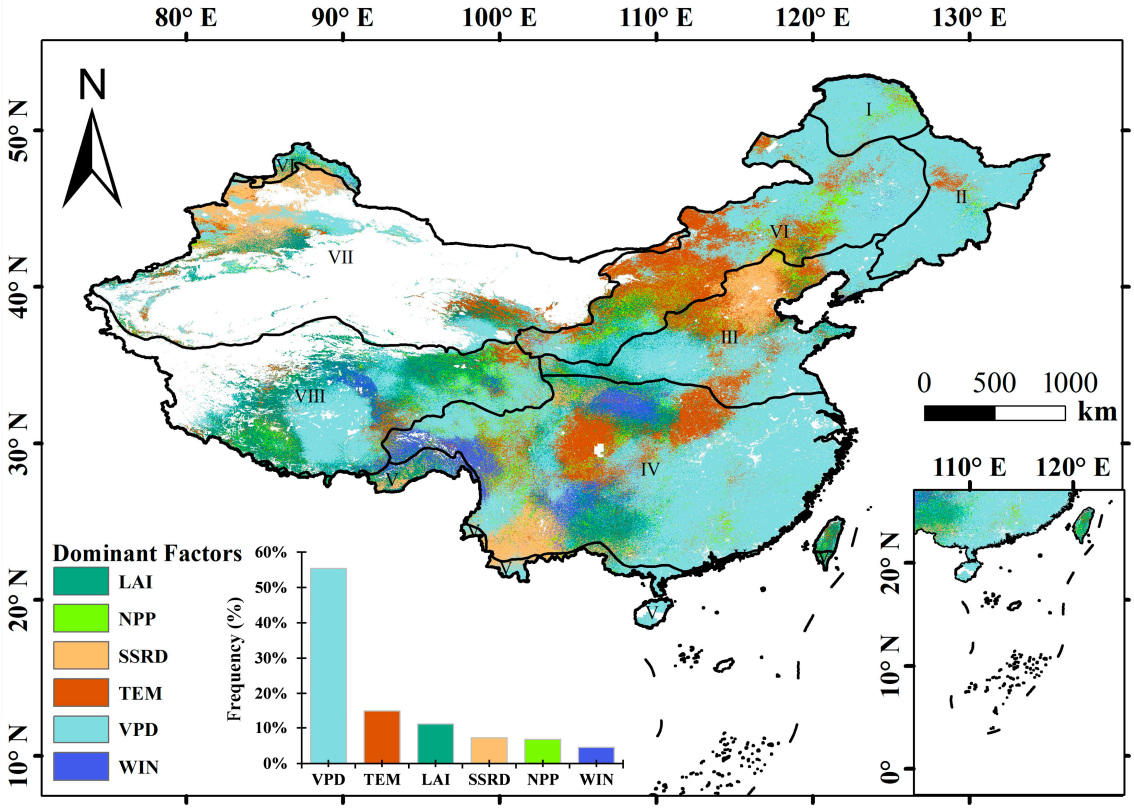

Figure 10. Spatial patterns of dominant factors related to NP changes in China.

In contrast, VPD (Figure 8f) was the largest negative driver, contributing to NP with a mean rate of −43.68% (Figure 9). VPD had a dominant influence on NP change in 55.39% of China (Figure 10), particularly in most of southern and eastern China. The mean contribution rate of VPD reached up to −50% in regions I and II (Figure 9).

Furthermore, WIN and SSRD exhibited a negative impact on NP, with a mean contribution rate of −4.27% and −6.67%, respectively (Figure 9). The negative impacts of SSRD (Figure 8e) were concentrated in Yunnan, Hebei, and the Junggar Basin, while those of WIN (Figure 8d) were observed in the Hanzhong Basin and southeastern Tibet. The positive influences were observed in specific regions only. SSRD exhibited a positive mean contribution rate in regions I and VIII, while WIN demonstrated a positive mean contribution rate in region VII (Figure 9).

The vegetation factors LAI and NPP exerted both positive and negative influences on NP, with mean contribution rates of 2.13% and −0.98%, respectively (Figure 9). The positive impacts of LAI (Figure 8a) were concentrated in southwestern China, whereas NPP (Figure 8b) was observed in northeastern China. These vegetation factors exerted a predominant influence on 11.07% and 6.77% of China, respectively (Figure 10).

With regard to the findings of the path analysis (Figure 11), it was found that SSRD had the largest direct negative impact in China, while NPP exhibited the highest direct positive impact. Among the six factors, TEM and WIN had similar direct negative effects on NP, whereas LAI and NPP demonstrated strong positive associations. At the regional scale, NPP exhibited the highest positive direct effect on regions I, III, and VII. The largest negative direct effect was demonstrated by SSRD on regions I, II, III, IV, VI, VII, and VIII. VPD exhibited the highest positive direct impact in region II, while in region V, it had a large negative direct impact. Additionally, LAI demonstrated a high negative direct effect on regions I, VII, and VIII, and a high positive direct effect on region VI. The greatest positive impact of TEM was observed in region V, while the greatest negative impact was observed in regions II and VIII.

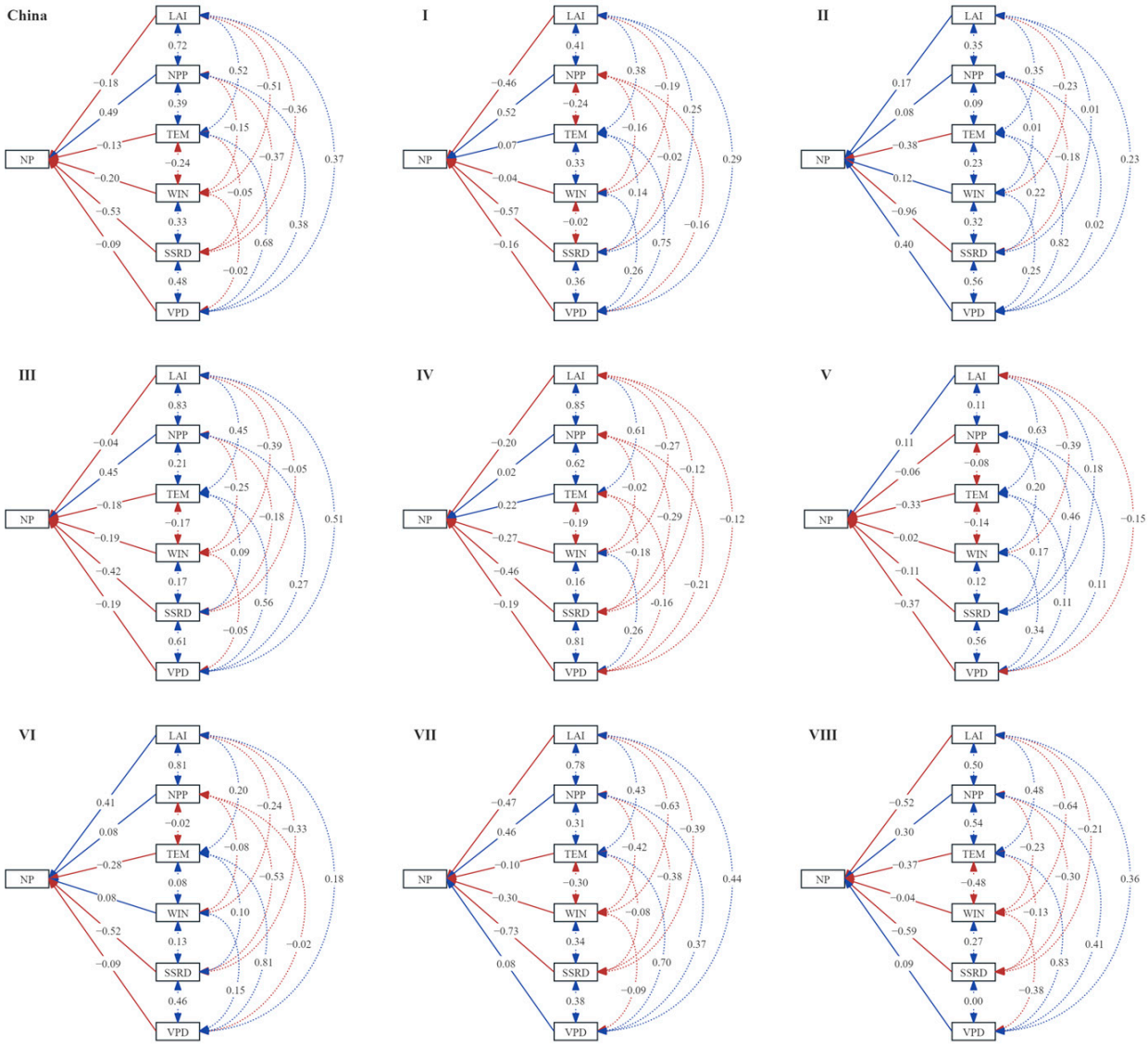

Figure 11. Path diagram of environmental factors and NP. Red and blue arrows indicate the negative and positive impacts, respectively. The solid and dashed lines typically represent direct and indirect relationships between variables, respectively. The numbers on each arrow denote the normalized path coefficients.

In the context of the combined effects of climate and vegetation factors on NP variation (Figure 12), climate changes were identified as the primary driver of changes in NP in approximately 61.53% of China. Within this category, 55.41% of regions exhibited negative changes, while 6.12% showed positive changes. The area percentage changes in NP, induced by vegetation factors and co-factors, were relatively similar. They accounted for 15.39% and 14.32%, respectively, and included both negative and positive impacts. Both climate and vegetation factors contribute to a higher area percentage of negative effects than positive effects on NP. In certain regions, climate factors were the main cause of the decrease in NP, while vegetation factors played a leading role in influencing both the decrease and increase in NP changes. Regions experiencing the joint influence of both climate and vegetation factors were scattered in northeastern parts of China.

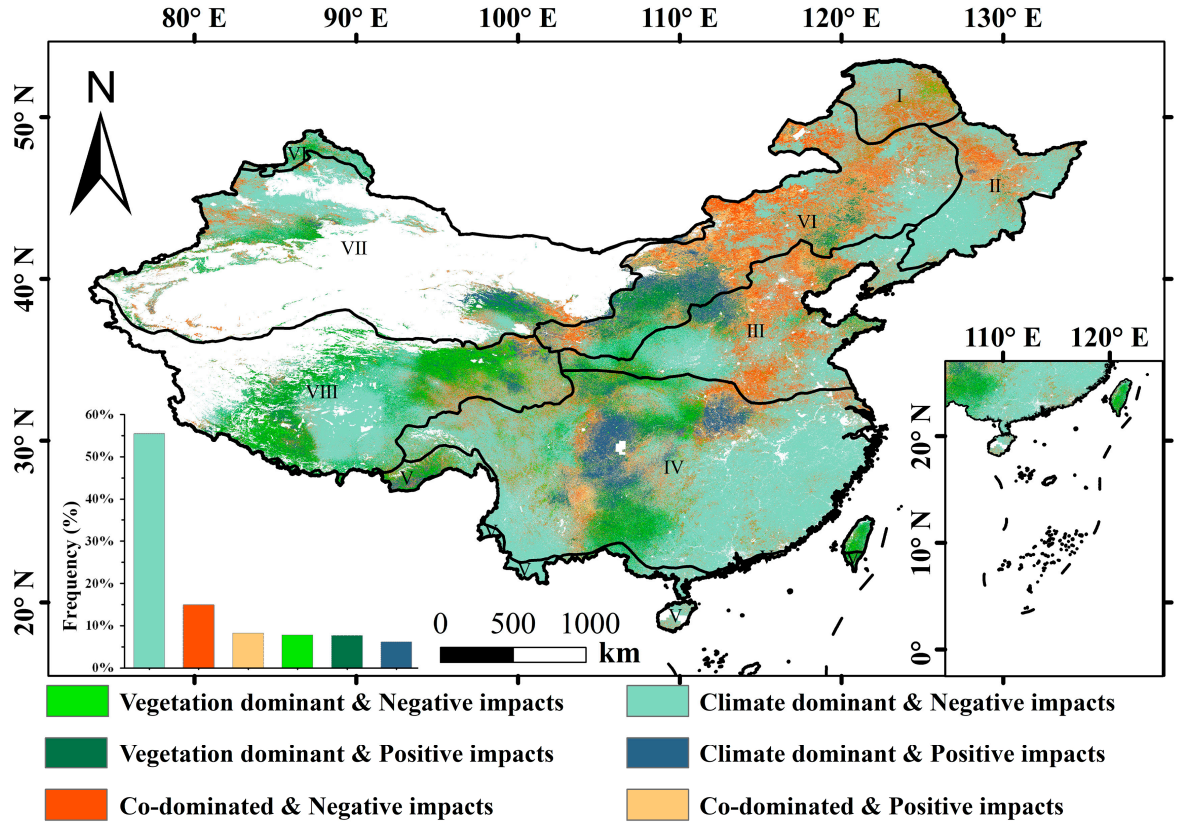

Figure 12. Spatial patterns of climate and vegetation factors dominating NP.

4. Discussion

Between 2001 and 2020 in China, we utilized the canopy water balance equation to indirectly measure the difference between PRE and EI, deriving NP. The PRE data were obtained from observational stations in China, while the sub-datasets of EI were sourced from PML ET datasets [43,50]. The performance of the PML model and datasets was validated using data from 95 flux towers globally, resulting in a Root Mean Square Error of 0.69 mm/day [43]. In this study, we decided not to use PRE data in the PML-V2 model due to concerns about the extension of the study area and data accuracy in China. Despite both data sources undergoing quality control [34,50], the inconsistency might still introduce uncertainty into NP estimation.

The multiyear annual mean NP was 674.62 mm (annual mean NP/PRE: 94.89%). However, comparative analyses with existing research show disparities. This value was found to be considerably higher than that observed in field experiments that were limited to specific locations and periods following the rainfall event. In China, Zhang et al. [39] found median Tf and Sf values of 74.3% and 2.7%, respectively. On a broader scale, Sadeghi et al. [5], based on 644 global observations, reported median relative Tf and Sf values of 75.8% and 2.2%. The values were derived from a quantitative synthesis of peer-reviewed papers based on site observation. Consequently, this value differs from previous studies, potentially due to scale gaps in time and space [39,45,48]. In our study, the mean NP/PRE ratio was employed as a means of reflecting the actual amount of precipitation that reached the ground over the course of the entire year. Additionally, the tendency for ecosystem-level Tf measurements to exceed those at the single/tree level may contribute to this discrepancy [9,51]. Nevertheless, when the value was compared with the EI interception rates obtained from a model based on remote sensing data over a long-term period at a global scale, the value was within the normal range. For instance, the EI rate obtained from a physics-informed hybrid machine learning was 8.6% [52]. He et al. [53] employed a Revised Gash Model, reporting an average annual ratio of EI to PRE of 22.30%

in China. The EI interception rates of different grassland types in the Qinghai-Tibet Plateau are as follows: alpine meadows, 3.11%; mountain meadows, 3.82%; temperate grassland, 2.45%; and temperate desert grassland, 1.13% [54]. Large-scale studies on EI suggest that the annual mean NP/PRE ranges from 70% to 99%.

The spatial pattern of NP was primarily influenced by the spatial distribution of precipitation and vegetation types [5,6]. Under the monsoon climate, precipitation decreased from southeast to northwest [55,56], which aligned with the distribution of NP. The seasonal NP in summer accounts for over 50% of the annual NP as the precipitation levels were significantly elevated. Furthermore, seasonal fluctuations in rainfall characteristics are accompanied by changes in tree canopy characteristics [40]. Consequently, the seasonal variability in precipitation might be as significant as the seasonal variability in leaf state. Vegetation types changed from tropical or subtropical forest to temperate steppe or temperate desert (Figure 1a), characterized by a sparser canopy structure that retained less rainwater [17,39]. In contrast, the spatial pattern of the NP/PRE ratio was found to be relatively low in the humid and semi-humid regions, with the lowest values in the northeast (Figure 3a). The annual NP/PRE ratio in this study reflected the influence of seasonal variability in vegetation and precipitation on the capacity of the canopy to intercept precipitation to some extent. The southern region generally had a higher comprehensive interception capacity of vegetation compared to the north [39]. The northern regions of VI, VII, and VIII in China were arid and semiarid areas with low NP values. These areas were dominated by shrubs, alpine, and desert vegetation types, and exhibited low vegetation coverage [39]. Exceptions in northern China include region I, which was a cold temperate coniferous forest, with low NP and NP/PRE values. The low amount of NP and the high interception ratio were attributed to the higher total plant leaf area of coniferous plants due to their needle leaf form [9,53]. According to Magliano et al. [4], the interception ratio in needle leaf form was higher than in broadleaf or pinnate leaf forms.

At the temporal scale, the annual mean NP, PRE, and EI in China exhibited a slight upward trend of 2.93 mm/yr, 3.39 mm/yr, and 1.63 mm/yr, respectively. This increase was consistent with the findings that interception, Tf, and Sf increase with rainfall event size [57]. The upward trend rate of EI was lower than that reported by He et al. [53] but higher than that reported by Yan et al. [58]. Although studies have reported an increase in precipitation amount and variability [33,34,55], 25% of regions have exhibited a decreasing trend in annual NP, primarily concentrated in southwestern China. At the regional level, only region V showed a decreasing trend in NP, potentially linked to a decrease in monsoon precipitation in southwest China [59], coupled with an increase in evapotranspiration in these regions [60].

In situ studies have shown that the amounts of NP depend on vegetation attributes, rainfall regime characteristics, and meteorological conditions [5,6,52]. Our findings indicate that, in most regions of China, it is PRE, rather than EI, that governs the interannual variation of NP, explaining approximately 68% of the NP trend. It was generally agreed that precipitation characteristics, represented by PRE, predominantly determine NP [57,61]. However, it overlooks other aspects of rainfall characteristics, such as duration, intensity, variation, and frequency [52]. Future research should incorporate these additional characteristics of rainfall events to enhance the understanding of the impact of changes in rainfall regime on NP, especially in regions with distinctive characteristics like dryland and low-vegetated areas in northwestern China [57,62].

To delve further into NP changes, we examined six additional climate and vegetation factors. Many previous studies have highlighted the pivotal role of VPD in regulating the trade-off between carbon and water fluxes [63,64]. During rainfall, VPD affected EI by influencing the difference in vapor pressure between wet surfaces and surrounding air. High VPD and dry air conditions tended to accelerate evaporation, whereas low VPD and humid conditions might have slowed down the process [42,65]. TEM influences NP through its regulation of PRE. As global temperatures rise, precipitation amount and variability continue to increase [33,34]. At the national level, TEM had a positive impact on NP in

China, particularly in northeastern regions, the Sichuan basin, and Huang-Huai-Hai Plain. These regions are affected by the East Asian monsoon, which is characterized by the influx of moist air from the Pacific Ocean during the summer [66,67]. This leads to increased evaporation and moisture, which in turn increases the likelihood of rainfall [68]. SSRD and WIN influence rainfall and subsequent processes of interception loss and evaporation. However, their contributions to NP in China at the yearly time scale were relatively modest in our study. In contrast to previous studies that emphasized the sensitivity of NP to wind magnitude at fine scales [5,6], the annual average WIN would alleviate the impact of extremely high wind speeds on NP. Additionally, the yearly averaged SSRD might temper the distinct seasonal and daily patterns in the relationship between solar radiation and evaporation [58,60].

To evaluate the influence of vegetation dynamics on NP changes, we identified LAI and NPP as key indicators. The national average contribution rate of NPP and LAI indicated that vegetation dynamics had a weak impact on NP changes in China. Previous studies have demonstrated that the characteristics of the vegetation community exert a significant influence on a small scale [7,27,69]. However, at a larger scale, meteorological factors such as precipitation characteristics, wind speed, and evaporation emerge as the dominant drivers [70]. Excluding the scale gap, the saturation phenomenon of the remote sensing-based vegetation index also leads to inaccuracies in estimating the vegetation growth status in densely vegetated areas [71,72]. Additionally, site-based studies underscore the importance of various canopy structure variables, including leaf shape, canopy thickness, size, and forms, in influencing rainfall redistribution processes [9,73,74]. Neglecting these structural properties of vegetation could potentially limit the accuracy of contributors for regional NP [17,39,73]. Therefore, future studies need to thoughtfully select vegetation variables characterizing biophysical properties, considering both data availability and accuracy.

5. Conclusions

This study investigated the dynamics of NP for different vegetation-type regions across China during 2001–2020 and analyzed the contribution of climate change and vegetation dynamics to the interannual variation in NP. The canopy water balance equation was employed to indirectly ascertain the discrepancy between PRE and EI, thereby deriving NP. The spatial distribution of NP exhibited a decreasing trend along the moisture gradient from southeast to northwest, in a manner analogous to that observed for precipitation across China. The NP/PRE ratio was found to be relatively low in the humid and semi-humid regions, exhibiting seasonal variability. This reflected the influence of seasonal variability in vegetation and precipitation on the capacity of the canopy to intercept precipitation. In general, the trend of NP has been on the rise over the past two decades, with an average change rate of 2.93 mm per year in China. This is due to a significant increase in precipitation during the summer and autumn seasons.

The contribution analysis revealed an increase in the trend of NP, with the spatiotemporal variations in NP being primarily attributed to changes in precipitation rather than EI. Notably, climate factors played a more dominant role in NP variation than vegetation factors in the majority of regions across China. The most significant factors influencing NP changes were VPD, TEM and LAI. The VPD exerted a negative influence on the southern and eastern regions. TEM and LAI exerted the most influence on the northeastern and southwestern regions, respectively. In conclusion, the results provide valuable insights into the pivotal role of climatic and vegetation factors in ecohydrological cycles. Further research should investigate the influence of vegetation characteristics, rainfall patterns and seasonality on the redistribution of rainfall.

Author Contributions: Conceptualization, J.C.; methodology, J.P., Y.J. and L.Y.; software, J.P.; validation, J.C. and J.P.; formal analysis, J.P. and Y.L.; investigation, Y.L. and J.P.; resources, L.Y. and Y.J.; data curation, J.P.; writing—original draft preparation, J.P.; writing—review and editing, Y.J. and J.C.;

visualization, J.P.; supervision, J.C.; project administration, J.C.; funding acquisition, J.C. All authors have read and agreed to the published version of the manuscript.

Funding: This research was funded by Chongqing Municipal Bureau of Water Resources (5"000002021BF40001, CQS23C01036), Central Guidance on Local Science and Technology Development Fund of Chongqing Municipality (2021000069/E1396207), and Chongqing Science and Technology project (CSTC2021jscx-gksbx0036).

Data Availability Statement: The PML-V2 ET (https://developers.google.com/earth-engine/datasets/catalog/CAS_IGSNRR_PML_V2_v017), MOD15A2H (https://developers.google.com/earth-engine/datasets/catalog/MODIS_061_MOD15A2H, accessed on 21 July 2023) and MOD17A3 (https://developers.google.com/earth-engine/datasets/catalog/MODIS_061_MOD17A3HGF, accessed on 21 July 2023) datasets could be downloaded from the GEE platform. Meteorological data were obtained from the China National Ground Meteorological Station Basic Meteorological Elements Daily Values Dataset (V3.0) (http://data.cma.cn/). SSRD data were obtained from the ECMWF ERA5-Land reanalysis dataset (https://www.ecmwf.int/en/era5-land). Physical Geographical Division data for China were obtained from the Resource and Environment Science and Data Center (https://www.resdc.cn). All datasets are publicly available and can be accessed via the links provided.

Acknowledgments: We acknowledge the research environment provided by Chongqing Institute of Green and Intelligent Technology, Chinese Academy of Sciences.

Conflicts of Interest: The authors declare no conflicts of interest.

References

1. David, J.S.; Valente, F.; Gash, J.H. Evaporation of Intercepted Rainfall. In *Encyclopedia of Hydrological Sciences*; John Wiley & Sons, Ltd.: Hoboken, NJ, USA, 2006; ISBN 978-0-47-084894-4.
2. Levia, D.F.; Keim, R.F.; Carlyle-Moses, D.E.; Frost, E.E. Throughfall and Stemflow in Wooded Ecosystems. In *Forest Hydrology and Biogeochemistry: Synthesis of Past Research and Future Directions*; Levia, D.F., Carlyle-Moses, D., Tanaka, T., Eds.; Ecological Studies; Springer: Dordrecht, The Netherlands, 2011; pp. 425–443. ISBN 978-9-40-071363-5.
3. McDowell, W.H.; Pérez-Rivera, K.X.; Shaw, M.E. Assessing the Ecological Significance of Throughfall in Forest Ecosystems. In *Forest-Water Interactions*; Levia, D.F., Carlyle-Moses, D.E., Iida, S., Michalzik, B., Nanko, K., Tischer, A., Eds.; Ecological Studies; Springer International Publishing: Cham, Switzerland, 2020; pp. 299–318. ISBN 978-3-03-026086-6.
4. Magliano, P.N.; Whitworth-Hulse, J.I.; Baldi, G. Interception, Throughfall and Stemflow Partition in Drylands: Global Synthesis and Meta-Analysis. *J. Hydrol.* **2019**, *568*, 638–645. [CrossRef]
5. Sadeghi, S.M.M.; Gordon, D.A.; Van Stan, J.T., II. A Global Synthesis of Throughfall and Stemflow Hydrometeorology. In *Precipitation Partitioning by Vegetation: A Global Synthesis*; Van Stan, I., John, T., Gutmann, E., Friesen, J., Eds.; Springer International Publishing: Cham, Switzerland, 2020; pp. 49–70. ISBN 978-3-03-029702-2.
6. Van Stan, J.T.; Hildebrandt, A.; Friesen, J.; Metzger, J.C.; Yankine, S.A. Spatial Variability and Temporal Stability of Local Net Precipitation Patterns. In *Precipitation Partitioning by Vegetation: A Global Synthesis*; Van Stan, I., John, T., Gutmann, E., Friesen, J., Eds.; Springer International Publishing: Cham, Switzerland, 2020; pp. 89–104. ISBN 978-3-03-029702-2.
7. Bruijnzeel, L.A.; Mulligan, M.; Scatena, F.N. Hydrometeorology of tropical montane cloud forests: Emerging patterns. *Hydrol. Processes* **2011**, *25*, 465–498. [CrossRef]
8. Schwärzel, K.; Ebermann, S.; Schalling, N. Evidence of Double-Funneling Effect of Beech Trees by Visualization of Flow Pathways Using Dye Tracer. *J. Hydrol.* **2012**, *470–471*, 184–192. [CrossRef]
9. Yue, K.; Frenne, P.; Fornara, D.; Meerbeek, K.; Li, W.; Peng, X.; Ni, X.; Peng, Y.; Wu, F.; Yang, Y.; et al. Global Patterns and Drivers of Rainfall Partitioning by Trees and Shrubs. *Glob. Chang. Biol.* **2021**, *27*, 3350–3357. [CrossRef] [PubMed]
10. Fischer-Bedtke, C.; Metzger, J.C.; Demir, G.; Wutzler, T.; Hildebrandt, A. Throughfall Spatial Patterns Translate into Spatial Patterns of Soil Moisture Dynamics—Empirical Evidence. *Hydrol. Earth Syst. Sci.* **2023**, *27*, 2899–2918. [CrossRef]
11. Parker, G.G. Throughfall and Stemflow in the Forest Nutrient Cycle. In *Advances in Ecological Research*; Elsevier: Amsterdam, The Netherlands, 1983; Volume 13, pp. 57–133. ISBN 978-0-12-013913-2.
12. Friesen, J. Flow Pathways of Throughfall and Stemflow Through the Subsurface. In *Precipitation Partitioning by Vegetation: A Global Synthesis*; Van Stan, I., John, T., Gutmann, E., Friesen, J., Eds.; Springer International Publishing: Cham, Switzerland, 2020; pp. 215–228. ISBN 978-3-03-029702-2.
13. Adriaenssens, S.; Hansen, K.; Staelens, J.; Wuyts, K.; De Schrijver, A.; Baeten, L.; Boeckx, P.; Samson, R.; Verheyen, K. Throughfall Deposition and Canopy Exchange Processes along a Vertical Gradient within the Canopy of Beech (*Fagus sylvatica* L.) and Norway Spruce (*Picea abies* (L.) Karst). *Sci. Total Environ.* **2012**, *420*, 168–182. [CrossRef] [PubMed]
14. Li, H.; Zhao, C.; Yang, G.; Feng, H. Variations in Crop Variables within Wheat Canopies and Responses of Canopy Spectral Characteristics and Derived Vegetation Indices to Different Vertical Leaf Layers and Spikes. *Remote Sens. Environ.* **2015**, *169*, 358–374. [CrossRef]

15. Zabret, K.; Šraj, M. Spatial Variability of Throughfall under Single Birch and Pine Tree Canopies. *Acta Hydrotech.* **2018**, *31*, 1–20. [CrossRef]
16. Miralles, D.G.; Gash, J.H.; Holmes, T.R.H.; de Jeu, R.A.M.; Dolman, A.J. Global Canopy Interception from Satellite Observations. *J. Geophys. Res. Atmos.* **2010**, *115*, 16122. [CrossRef]
17. Porada, P.; Van Stan, J.T.; Kleidon, A. Significant Contribution of Non-Vascular Vegetation to Global Rainfall Interception. *Nat. Geosci.* **2018**, *11*, 563–567. [CrossRef]
18. Zhang, Y.; Yuan, C.; Chen, N.; Levia, D.F. Rainfall Partitioning by Vegetation in China: A Quantitative Synthesis. *J. Hydrol.* **2023**, *617*, 128946. [CrossRef]
19. Carlyle-Moses, D.E. Throughfall, Stemflow, and Canopy Interception Loss Fluxes in a Semi-Arid Sierra Madre Oriental Matorral Community. *J. Arid. Environ.* **2004**, *58*, 181–202. [CrossRef]
20. Ponette-González, A.G.; Van Stan, J.T., II; Magyar, D. Things Seen and Unseen in Throughfall and Stemflow. In *Precipitation Partitioning by Vegetation: A Global Synthesis*; Van Stan, I., John, T., Gutmann, E., Friesen, J., Eds.; Springer International Publishing: Cham, Switzerland, 2020; pp. 71–88. ISBN 978-3-03-029702-2.
21. Antoneli, V.; de Jesus, F.C.; Bednarz, J.A.; Thomaz, E.L. Stemflow and Throughfall in Agricultural Crops: A Synthesis. *Rev. Ambient. Água* **2021**, *16*, e2528. [CrossRef]
22. Inkiläinen, E.N.M.; McHale, M.R.; Blank, G.B.; James, A.L.; Nikinmaa, E. The Role of the Residential Urban Forest in Regulating Throughfall: A Case Study in Raleigh, North Carolina, USA. *Landsc. Urban Plan.* **2013**, *119*, 91–103. [CrossRef]
23. Zabret, K.; Šraj, M. Rainfall Interception by Urban Trees and Their Impact on Potential Surface Runoff. *CLEAN–Soil Air Water* **2019**, *47*, 1800327. [CrossRef]
24. Kundu, S.; Khare, D.; Mondal, A. Past, Present and Future Land Use Changes and Their Impact on Water Balance. *J. Environ. Manag.* **2017**, *197*, 582–596. [CrossRef] [PubMed]
25. Gerrits, A.M.J.; Pfister, L.; Savenije, H.H.G. Spatial and Temporal Variability of Canopy and Forest Floor Interception in a Beech Forest. *Hydrol. Process.* **2010**, *24*, 3011–3025. [CrossRef]
26. Sadeghi, S.M.M.; Attarod, P.; Van Stan, J.T.; Pypker, T.G.; Dunkerley, D. Efficiency of the Reformulated Gash's Interception Model in Semiarid Afforestations. *Agric. For. Meteorol.* **2015**, *201*, 76–85. [CrossRef]
27. Muzylo, A.; Llorens, P.; Valente, F.; Keizer, J.J.; Domingo, F.; Gash, J.H.C. A Review of Rainfall Interception Modelling. *J. Hydrol.* **2009**, *370*, 191–206. [CrossRef]
28. Vrugt, J.A.; Dekker, S.C.; Bouten, W. Identification of Rainfall Interception Model Parameters from Measurements of Throughfall and Forest Canopy Storage. *Water Resour. Res.* **2003**, *39*, 1251. [CrossRef]
29. Sadeghi, S.M.M.; Van Stan, J.T.; Pypker, T.G.; Tamjidi, J.; Friesen, J.; Farahnaklangroudi, M. Importance of Transitional Leaf States in Canopy Rainfall Partitioning Dynamics. *Eur. J. For. Res.* **2018**, *137*, 121–130. [CrossRef]
30. Tang, Q.; Yin, Y.; Zhang, X.; Zhu, T.; Zhao, J.; Yang, W. Geography of China. In *Atlas of Environmental Risks Facing China under Climate Change*; Tang, Q., Ge, Q., Eds.; IHDP/Future Earth-Integrated Risk Governance Project Series; Springer: Singapore, 2018; pp. 1–20. ISBN 978-9-81-104199-0.
31. Chen, C.; Park, T.; Wang, X.; Piao, S.; Xu, B.; Chaturvedi, R.K.; Fuchs, R.; Brovkin, V.; Ciais, P.; Fensholt, R.; et al. China and India Lead in Greening of the World through Land-Use Management. *Nat. Sustain.* **2019**, *2*, 122–129. [CrossRef] [PubMed]
32. Piao, S.; Wang, X.; Park, T.; Chen, C.; Lian, X.; He, Y.; Bjerke, J.W.; Chen, A.; Ciais, P.; Tømmervik, H.; et al. Characteristics, Drivers and Feedbacks of Global Greening. *Nat. Rev. Earth Environ.* **2020**, *1*, 14–27. [CrossRef]
33. Pendergrass, A.G.; Knutti, R.; Lehner, F.; Deser, C.; Sanderson, B.M. Precipitation Variability Increases in a Warmer Climate. *Sci. Rep.* **2017**, *7*, 17966. [CrossRef] [PubMed]
34. Zhang, W.; Furtado, K.; Wu, P. Increasing Precipitation Variability on Daily-to-Multiyear Time Scales in a Warmer World. Available online: https://www.science.org/doi/10.1126/sciadv.abf8021 (accessed on 4 November 2023).
35. Li, Y.; Chen, P.; Niu, Y.; Liang, Y.; Wei, T. Dynamics and Attributions of Ecosystem Water Yields in China from 2001 to 2020. *Ecol. Indic.* **2022**, *143*, 109373. [CrossRef]
36. Winkler, K.; Fuchs, R.; Rounsevell, M.; Herold, M. Global Land Use Changes Are Four Times Greater than Previously Estimated. *Nat. Commun.* **2021**, *12*, 2501. [CrossRef]
37. Zhu, X.; He, Z.; Du, J.; Chen, L.; Lin, P.; Tian, Q. Spatial Heterogeneity of Throughfall and Its Contributions to the Variability in Near-Surface Soil Water-Content in Semiarid Mountains of China. *For. Ecol. Manag.* **2021**, *488*, 119008. [CrossRef]
38. Zheng, J.; Fan, J.; Zhang, F.; Yan, S.; Xiang, Y. Rainfall Partitioning into Throughfall, Stemflow and Interception Loss by Maize Canopy on the Semi-Arid Loess Plateau of China. *Agric. Water Manag.* **2018**, *195*, 25–36. [CrossRef]
39. Zhang, Q.; Lv, X.; Yu, X.; Ni, Y.; Ma, L.; Liu, Z. Species and Spatial Differences in Vegetation Rainfall Interception Capacity: A Synthesis and Meta-Analysis in China. *CATENA* **2022**, *213*, 106223. [CrossRef]
40. Bai, P. Comparison of Remote Sensing Evapotranspiration Models: Consistency, Merits, and Pitfalls. *J. Hydrol.* **2023**, *617*, 128856. [CrossRef]
41. Leuning, R.; Zhang, Y.Q.; Rajaud, A.; Cleugh, H.; Tu, K. A Simple Surface Conductance Model to Estimate Regional Evaporation Using MODIS Leaf Area Index and the Penman-Monteith Equation. *Water Resour. Res.* **2008**, *44*, 10419. [CrossRef]
42. Monteith, J.L. Evaporation and Environment. *Symp. Soc. Exp. Biol.* **1965**, *19*, 205–234.
43. Zhang, Y.; Kong, D.; Gan, R.; Chiew, F.H.S.; McVicar, T.R.; Zhang, Q.; Yang, Y. Coupled Estimation of 500 m and 8-Day Resolution Global Evapotranspiration and Gross Primary Production in 2002–2017. *Remote Sens. Environ.* **2019**, *222*, 165–182. [CrossRef]

44. Zhang, Y.; Peña-Arancibia, J.L.; McVicar, T.R.; Chiew, F.H.S.; Vaze, J.; Liu, C.; Lu, X.; Zheng, H.; Wang, Y.; Liu, Y.Y.; et al. Multi-Decadal Trends in Global Terrestrial Evapotranspiration and Its Components. *Sci. Rep.* **2016**, *6*, 19124. [CrossRef]
45. Tobon, C.; Bouten, W.; Sevink, J. Gross Rainfall and Its Partitioning into Throughfall, Stemflow and Evaporation of Intercepted Water in Four Forest Ecosystems in Western Amazonia. *J. Hydrol.* **2000**, *237*, 40–57. [CrossRef]
46. Ge, W.; Deng, L.; Wang, F.; Han, J. Quantifying the Contributions of Human Activities and Climate Change to Vegetation Net Primary Productivity Dynamics in China from 2001 to 2016. *Sci. Total Environ.* **2021**, *773*, 145648. [CrossRef]
47. Yang, S.; Zhang, J.; Wang, J.; Zhang, S.; Bai, Y.; Shi, S.; Cao, D. Spatiotemporal Variations of Water Productivity for Cropland and Driving Factors over China during 2001–2015. *Agric. Water Manag.* **2022**, *262*, 107328. [CrossRef]
48. Walker, E.D.; Hart, J.E.; Koutrakis, P.; Cavallari, J.M.; VoPham, T.; Luna, M.; Laden, F. Spatial and Temporal Determinants of A-Weighted and Frequency Specific Sound Levels—An Elastic Net Approach. *Environ. Res.* **2017**, *159*, 491–499. [CrossRef]
49. Zhang, Z.; Lai, Z.; Xu, Y.; Shao, L.; Wu, J.; Xie, G.-S. Discriminative Elastic-Net Regularized Linear Regression. *IEEE Trans. Image Process.* **2017**, *26*, 1466–1481. [CrossRef]
50. He, S.; Zhang, Y.; Ma, N.; Tian, J.; Kong, D.; Liu, C. A Daily and 500 m Coupled Evapotranspiration and Gross Primary Production Product across China during 2000–2020. *Earth Syst. Sci. Data* **2022**, *14*, 5463–5488. [CrossRef]
51. Levia, D.F.; Frost, E.E. Variability of Throughfall Volume and Solute Inputs in Wooded Ecosystems. *Prog. Phys. Geogr. Earth Environ.* **2006**, *30*, 605–632. [CrossRef]
52. Lian, X.; Zhao, W.; Gentine, P. Recent Global Decline in Rainfall Interception Loss Due to Altered Rainfall Regimes. *Nat. Commun.* **2022**, *13*, 7642. [CrossRef]
53. He, W.; Jing, Y.; Jiang, Z.-Y.; Liao, C.-M.; Yu, Y.; Peng, J.-H.; Zhang, Y.-D.; Hou, G.-L.; Zhang, S.-Y. Spatiotemporal Variations in Vegetation Canopy Interception in China Based on a Revised Gash Model. *Forests* **2022**, *13*, 1404. [CrossRef]
54. Liu, Y.; Wu, J.; Li, C. Model Simulation of Vegetation Canopy Precipitation Interception in Grassland Ecosystems on the Northeast Margin of the Qinghai-Tibet Plateau. *Ecol. Model.* **2024**, *488*, 110576. [CrossRef]
55. Guo, B.; Zhang, J.; Meng, X.; Xu, T.; Song, Y. Long-Term Spatio-Temporal Precipitation Variations in China with Precipitation Surface Interpolated by ANUSPLIN. *Sci. Rep.* **2020**, *10*, 81. [CrossRef]
56. Harka, A.E.; Jilo, N.B.; Behulu, F. Spatial-Temporal Rainfall Trend and Variability Assessment in the Upper Wabe Shebelle River Basin, Ethiopia: Application of Innovative Trend Analysis Method. *J. Hydrol. Reg. Stud.* **2021**, *37*, 100915. [CrossRef]
57. Magliano, P.N.; Whitworth-Hulse, J.I.; Cid, F.D.; Leporati, J.L.; Van Stan, J.T.; Jobbágy, E.G. Global Rainfall Partitioning by Dryland Vegetation: Developing General Empirical Models. *J. Hydrol.* **2022**, *607*, 127540. [CrossRef]
58. Yan, L.; Chen, J.; He, L.; Ji, Y.; Tang, Q.; Fan, Y.; Tan, D. Dynamics of the Evaporation of Intercepted Precipitation during the Last Two Decades over China. *Remote Sens.* **2022**, *14*, 2474. [CrossRef]
59. Tan, L.; Cai, Y.; An, Z.; Cheng, H.; Shen, C.C.; Gao, Y.; Edwards, R.L. Decreasing Monsoon Precipitation in Southwest China during the Last 240 Years Associated with the Warming of Tropical Ocean. *Clim. Dyn.* **2017**, *48*, 1769–1778. [CrossRef]
60. Zhang, J.; Zhou, X.; Yang, S.; Ao, Y. Spatiotemporal Variations in Evapotranspiration and Their Driving Factors in Southwest China between 2003 and 2020. *Remote Sens.* **2023**, *15*, 4418. [CrossRef]
61. Zhang, Y.; Wang, X.; Pan, Y.; Hu, R.; Chen, N. Global Quantitative Synthesis of Effects of Biotic and Abiotic Factors on Stemflow Production in Woody Ecosystems. *Glob. Ecol. Biogeogr.* **2021**, *30*, 1713–1723. [CrossRef]
62. Morillas, L.; Leuning, R.; Villagarcía, L.; García, M.; Serrano-Ortiz, P.; Domingo, F. Improving Evapotranspiration Estimates in Mediterranean Drylands: The Role of Soil Evaporation. *Water Resour. Res.* **2013**, *49*, 6572–6586. [CrossRef]
63. Zhang, S.; Tao, F.; Zhang, Z. Spatial and Temporal Changes in Vapor Pressure Deficit and Their Impacts on Crop Yields in China during 1980–2008. *J. Meteorol. Res.* **2017**, *31*, 800–808. [CrossRef]
64. Zhong, Z.; He, B.; Wang, Y.-P.; Chen, H.W.; Chen, D.; Fu, Y.H.; Chen, Y.; Guo, L.; Deng, Y.; Huang, L.; et al. Disentangling the Effects of Vapor Pressure Deficit on Northern Terrestrial Vegetation Productivity. *Sci. Adv.* **2023**, *9*, eadf3166. [CrossRef] [PubMed]
65. Ball, J.T.; Woodrow, I.E.; Berry, J.A. A Model Predicting Stomatal Conductance and Its Contribution to the Control of Photosynthesis under Different Environmental Conditions. In *Progress in Photosynthesis Research: Volume 4, Proceedings of the VIIth International Congress on Photosynthesis Providence, Rhode Island, USA, 10–15 August 1986*; Biggins, J., Ed.; Springer: Dordrecht, The Netherlands, 1987; pp. 221–224. ISBN 978-9-40-170519-6.
66. Fang, J.; Piao, S.; Zhou, L.; He, J.; Wei, F.; Myneni, R.B.; Tucker, C.J.; Tan, K. Precipitation Patterns Alter Growth of Temperate Vegetation. *Geophys. Res. Lett.* **2005**, *32*, 21411. [CrossRef]
67. Cui, Y.; Jia, L.; Fan, W. Estimation of Actual Evapotranspiration and Its Components in an Irrigated Area by Integrating the Shuttleworth-Wallace and Surface Temperature-Vegetation Index Schemes Using the Particle Swarm Optimization Algorithm. *Agric. For. Meteorol.* **2021**, *307*, 108488. [CrossRef]
68. Ge, S.; Jiang, C.; Wang, J.; Liu, S. Analyzing Temperature and Precipitation Extremes in China Using Multiple Gridded Datasets: A Comparative Evaluation. *Weather Clim. Extrem.* **2023**, *42*, 100614. [CrossRef]
69. Blume, T.; Schneider, L.; Güntner, A. Comparative Analysis of Throughfall Observations in Six Different Forest Stands: Influence of Seasons, Rainfall- and Stand Characteristics. *Hydrol. Process.* **2022**, *36*, e14461. [CrossRef]
70. Fleischbein, K.; Wilcke, W.; Goller, R.; Boy, J.; Valarezo, C.; Zech, W.; Knoblich, K. Rainfall Interception in a Lower Montane Forest in Ecuador: Effects of Canopy Properties. *Hydrol. Process.* **2005**, *19*, 1355–1371. [CrossRef]
71. Mutanga, O.; Masenyama, A.; Sibanda, M. Spectral Saturation in the Remote Sensing of High-Density Vegetation Traits: A Systematic Review of Progress, Challenges, and Prospects. *ISPRS J. Photogramm. Remote Sens.* **2023**, *198*, 297–309. [CrossRef]

72. Zhang, Y.; Leuning, R.; Hutley, L.B.; Beringer, J.; McHugh, I.; Walker, J.P. Using Long-Term Water Balances to Parameterize Surface Conductances and Calculate Evaporation at 0.05° Spatial Resolution. *Water Resour. Res.* **2010**, *46*, 05512. [CrossRef]
73. Fang, H.; Li, S.; Zhang, Y.; Wei, S.; Wang, Y. New Insights of Global Vegetation Structural Properties through an Analysis of Canopy Clumping Index, Fractional Vegetation Cover, and Leaf Area Index. *Sci. Remote Sens.* **2021**, *4*, 100027. [CrossRef]
74. Tu, L.; Xiong, W.; Wang, Y.; Yu, P.; Liu, Z.; Han, X.; Yu, Y.; Shi, Z.; Guo, H.; Li, Z.; et al. Integrated Effects of Rainfall Regime and Canopy Structure on Interception Loss: A Comparative Modelling Analysis for an Artificial Larch Forest. *Ecohydrology* **2021**, *14*, e2283. [CrossRef]